This is a copy of the published version, or version of record, available on the publisher's website. This version does not track changes, errata, or withdrawals on the publisher's site.

Methods for extremely sparse-angle proton tomography

B. T. Spiers, R. Aboushelbaya, Q. Feng, M. W. Mayr, I. Ouatu, R. W. Paddock, R. Timmis, R. H.-W. Wang, and P. A. Norreys

Published version information

Citation: BT Spiers et al. Methods for extremely sparse-angle proton tomography. Phys Rev E 104, no. 4 (2021): 045201

DOI: 10.1103/PhysRevE.104.045201

This version is made available in accordance with publisher policies. Please cite only the published version using the reference above. This is the citation assigned by the publisher at the time of issuing the APV. Please check the publisher's website for any updates.

This item was retrieved from **ePubs**, the Open Access archive of the Science and Technology Facilities Council, UK. Please contact epublications@stfc.ac.uk or go to http://epubs.stfc.ac.uk/ for further information and policies.

Methods for extremely sparse-angle proton tomography

B. T. Spiers,[1,*] R. Aboushelbaya,[1] Q. Feng,[1] M. W. Mayr,[1] I. Ouatu,[1] R. W. Paddock,[1] R. Timmis,[1] R. H.-W. Wang,[1] and P. A. Norreys[1,2,3]

[1]*Department of Physics, Atomic and Laser Physics sub-Department, University of Oxford, Clarendon Laboratory, Oxford OX1 3PU, United Kingdom*

[2]*Central Laser Facility, UKRI-STFC Rutherford Appleton Laboratory, Harwell Campus, Didcot, Oxfordshire OX11 0QX, United Kingdom*

[3]*John Adams Institute, Denys Wilkinson Building, Oxford OX1 3RH, United Kingdom*

(Received 25 March 2021; revised 21 June 2021; accepted 18 August 2021; published 7 October 2021)

Proton radiography is a widely fielded diagnostic used to measure magnetic structures in plasma. The deflection of protons with multi-MeV kinetic energy by the magnetic fields is used to infer their path-integrated field strength. Here the use of tomographic methods is proposed for the first time to lift the degeneracy inherent in these path-integrated measurements, allowing full reconstruction of spatially resolved magnetic field structures in three dimensions. Two techniques are proposed which improve the performance of tomographic reconstruction algorithms in cases with severely limited numbers of available probe beams, as is the case in laser-plasma interaction experiments where the probes are created by short, high-power laser pulse irradiation of secondary foil targets. A new configuration allowing production of more proton beams from a single short laser pulse is also presented and proposed for use in tandem with these analytical advancements.

DOI: 10.1103/PhysRevE.104.045201

I. INTRODUCTION

The proton radiography diagnostic allows probing of transient and quasistatic magnetic field structures in plasmas [1,2]. It has been used to image magnetic fields in laboratory analogs of astrophysical collisionless shocks [3–5], the Weibel instability in interpenetrating plasma flows [6], stochastic magnetic fields amplified by the turbulent dynamo mechanism [7], and fields involved in laser-driven magnetic reconnection [8,9]. In the higher-density physics regime, proton radiography has been used to probe plasma fields in imploding inertial fusion capsules in both direct-drive [10–12] and indirect-drive laser-hohlraum [13–15] configurations and in studies of laser channelling physics relevant to fast ignition [16]. Proton-radiographic magnetic field measurements have also been used to validate a Faraday rotation-based magnetic field diagnostic at OMEGA [17].

A laser-generated proton beam [18] is directed through a plasma and is deflected as it propagates by local electromagnetic field structures. After exiting the plasma, the beam propagates over a distance before impinging on a detector screen. CR-39 and radiochromic film are commonly used as proton detectors and each has its own advantages and disadvantages [19].

While the resulting images are difficult to relate directly to the fields in the plama [20], theoretical work from [21] and [22] present algorithms which are able to recover transverse magnetic field components, path-integrated along the directions of proton probing. More recently, [23] developed a statistical approach to compensate for lack of information regarding the transverse profile of the proton beam prior to interaction with the plasma. [24] investigated the application of machine learning methods to the problem of proton radiography inversion, noting the degeneracy involved in interpreting path-integrated measurements, and suggested taking proton radiographs from multiple view angles as a method for resolving field structures spatially. While some experiments—for example those of [25] and more recently [9]—have probed similar interactions along different axes, the first full exploration of the possibility of recovering spatially resolved magnetic field structures from proton radiographs using standard tomography techniques is presented here.

Volegov *et al.* have pioneered the use of tomographic techniques in three-dimensional reconstruction of plasma parameters at the National Ingition Facility [26–29]. They employ a number of approaches using different probing geometries with orthogonal basis function representations (such as spherical and cylindrical harmonic decompositions) of the function under observation. We refine this approach and investigate its application to data extracted from proton radiography observations of electromagnetic fields.

In Sec. II a brief summary of proton radiography is presented, along with a description of a current state-of-the-art pipeline for analysis. The reader is then introduced to the subject of tomography in Sec. III, along with the *filtered back-projection* algorithm (FBP), which is one of the most important and widely used in tomography applications. In Sec. IV an approach to tomography using Fourier decomposition in the angular variable is presented. When implemented in this way the new approach is realized by an interpolation in observation angle. Section V presents another new method, which improves reconstruction quality of functions with much larger extent in one dimension than the others by making them

*benjamin.spiers@physics.ox.ac.uk

 ©2021 American Physical Society

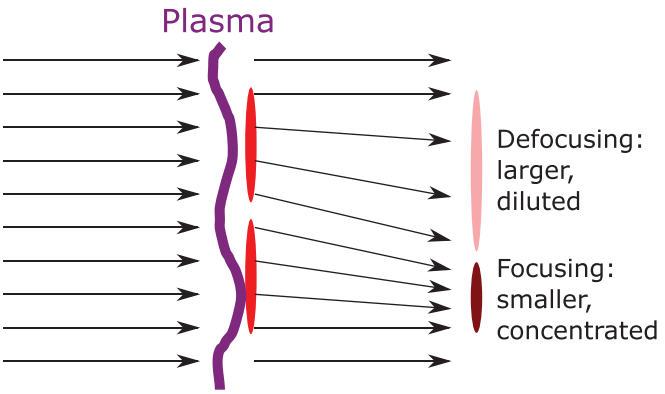

FIG. 1. Schematic of the mechanism by which proton radiography images are formed. Protons velocities are deviated downwards, most strongly in the center of the plasma and more weakly toward the edges. This causes protons which have traversed the lower half of the plasma to be "focused" and those which have traversed the upper half to be "defocused." The defocusing region appears larger at the image plane than the focusing region due to the divergence of velocities in that region.

appear "squashed" into a more uniform aspect ratio before a reconstruction algorithm is used. In Sec. VI it is shown how these modifications improve the quality of reconstruction for a function representing the magnetic field of a plasma channel, and the experimental realization of the proposed scheme is discussed. Section VII summarizes the results, illustrates areas for further research, and concludes the article.

II. PROTON RADIOGRAPHY

Proton radiography, in the limit of paraxiality and small in-plasma deflections, can be understood as a measurement of the electromagnetic fields present in plasma along a set of parallel, straight lines. Considering for example a probe direction aligned with the z direction, the diagnostic measures a combination of transverse electric and magnetic field components in the x and y directions [20]. These are encoded in the deflection of particles from otherwise straight-line paths by the transverse components of the Lorentz force, i.e., $\Delta v_x \propto \int E_x - v_0 B_y z$ for protons with initial velocity v_0 and similarly for Δv_y.

Deflections of particles are not directly detected; rather, the proton fluence is recorded on a detector such as CR-39 or radiochromic film [19]. This quantity is increased in regions of the image plane where proton velocities converge and decreased in regions where they diverge, relative to the flat-field fluence which would be measured in the absence of deflections.

Recovering the deflections imparted by the plasma is complicated by the fact that as well as increasing the proton fluence, the convergence of proton trajectories causes a reduction in the apparent size of such regions. Correspondingly, regions of diverging trajectories appear larger as well as being decreased in fluence. A schematic of this process is presented in Fig. 1. Algorithms which account for this effect can effectively recover the proton deflections necessary to produce an observed fluence distribution from a given source fluence distribution, though importantly for them to work the trajectories of protons must not cross before reaching the detector, forming caustics [22]. Statistical techniques further enable use of these algorithms in the absence of known initial fluence distribution [23].

It should be stressed that these algorithms formally recover the *deflections* of protons at the image plane and are agnostic toward the physics causing these deflections. Therefore a model is employed to calculate the values of electromagnetic fields which produced the recovered deflections. In particular the partition of electric vs. magnetic fields is an important unknown quantity, and several techniques have been suggested to separate these.

A simple model is the approximation that fast processes in plasma (such as laser channelling) can generate persistent magnetic field structures while the associated electric fields decay on much shorter timescales as the plasma restores quasineutrality [16,30]. Therefore the observed proton deflections are dominated by the magnetic contribution when the probing is at sufficiently late times. A more sophisticated approach which exploits the different energy dependence of deflections caused by electric or magnetic fields was proposed by [31] and can be used to disambiguate the two contributions where the proton source has at least two well-defined energies. This is especially applicable in the case of implosion capsule proton sources such as those described by [32], due to their two-peaked energy spectrum.

The discussion of this section suggests the following pipeline for analysis of proton radiography images: First, detector calibrations should be used to determine the proton fluence present on the detector from a scanned image. Then these fluences are fed into a Monge-Ampère solver such as PROBLEM [33] which determines the proton deflections imparted by the plasma, employing methods such as that of [23] to account for source profiles if necessary. These deflections are then decomposed into electric and magnetic field components, transverse to the probe direction.

Even in ideal scenarios, this reconstruction pipeline will only produce information about line-integrated fields. Symmetry assumptions may be used to make conclusions about the three-dimensional distribution of fields (for example, using Abel transform inversion if the plasma is known to have an axis of symmetry), and [24] proposed that the additional information available when taking proton radiographs from multiple different probe directions could enable full reconstruction of three-dimensional fields. This poses a *vector tomography problem*, in the most general case for each of the electric and magnetic fields. The next section focuses on reconstruction of magnetic field components, as these are more commonly studied using proton radiography, but the same arguments can also be applied to reconstruction of electric fields.

III. TOMOGRAPHY

A. Basic theory of tomography

In this work the proton source-plasma distance assumed to be sufficiently large compared to the transverse extent of the plasma that proton trajectories entering the plasma are

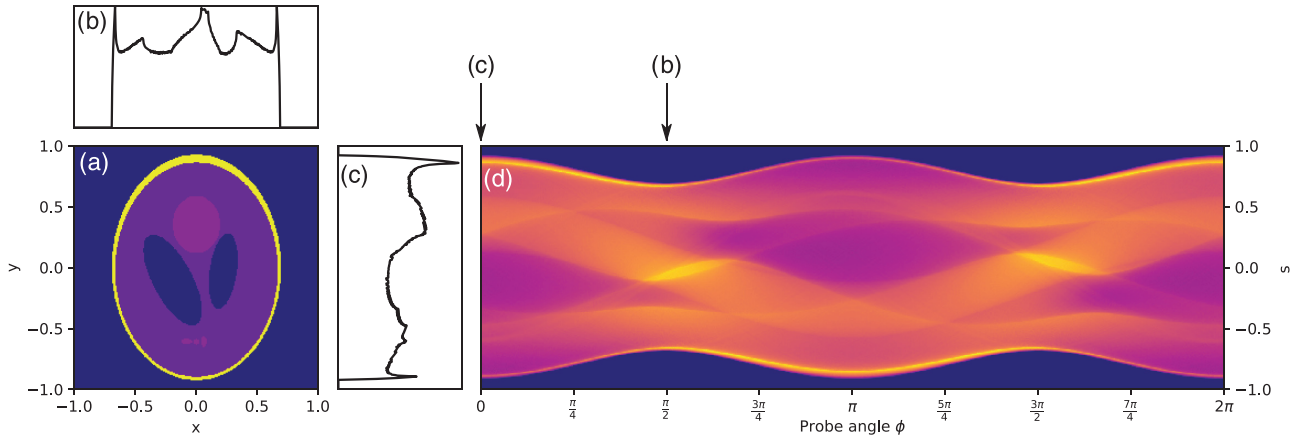

FIG. 2. (a): The Shepp-Logan phantom $f(x, y)$ and its sinogram $F(\phi, s)$ (d). [(b) and c)] Projections of f along the y and x axes, respectively, corresponding to $F(\frac{\pi}{2}, s)$ and $F(0, s)$. Note that F is 2π-periodic and has the parity property $F(\phi + \pi, s) = F(\phi, -s)$.

effectively paraxial, as this allows us to consider *parallel-probe* tomography (i.e., tomography in which each observation is made using a collimated beam).

A three-dimensional scalar function $f(x, y, z)$ is defined in Cartesian coordinates. A tomographic projection of this function is parametrized by the probe angle θ. For a given θ we define a new Cartesian coordinate system ("projection coordinates") (q, s, t) related to the "lab coordinates" (x, y, z) by rotation about the z axis:

$$\begin{bmatrix} q \\ s \\ t \end{bmatrix} = \begin{bmatrix} x\cos\theta + y\sin\theta \\ y\cos\theta - x\sin\theta \\ z \end{bmatrix}, \tag{1}$$

$$\begin{bmatrix} x \\ y \\ z \end{bmatrix} = \begin{bmatrix} q\cos\theta - s\sin\theta \\ s\cos\theta + q\sin\theta \\ t \end{bmatrix}. \tag{2}$$

Taking projections along the local q direction produces for each θ a function of s and t:

$$\begin{aligned} F_\theta(s,t) &= \int_{-\infty}^{\infty} f(x(q,s), y(q,s), t)q \\ &= \mathcal{R}_\theta[f(x,y,z)](s,t) \\ &= \mathcal{R}_\theta[f(x,y,t)](s). \end{aligned} \tag{3}$$

This equation defines the Radon transform $\mathcal{R}_\theta$, the integral transform that is the theoretical basis of tomographic analysis. It is important to note that, due to our assumption of parallel probing, this is effectively a "stack" of two-dimensional tomographs, one for each value in t. The values of $F_\theta(s, t)$ at fixed t are only influenced by the two-dimensional slice of the original function for which $z = t$: $f(x, y, t)$, for all s and θ. This allows for application of two-dimensional inversion algorithms to the three-dimensional tomography problem.

The function $F_\theta(s)$ (whose dependence on t has been dropped following the previous argument) is often visualized as a "sinogram": The parameter θ is promoted to a variable and the resulting two-variable function $F(s, \theta)$ is plotted as an image. An example of a sinogram is shown in Fig. 2. This sinogram was computed from the Shepp-Logan phantom, a function often used to test tomographic techniques [34]. A modified version of the Shepp-Logan phantom with both positive and negative values is employed in the following sections, as this better represents the nature of magnetic field structures.

It is in general possible to perform tomographic measurements without the restriction of all probe directions to a common plane (equivalently, without a single well-defined "axis of rotation") [28]. In that case, however, the choice of reconstruction methods is more limited. As discussed in the next section, sampling without a well-defined axis of rotation is not useful for magnetic field tomography, so methods involving this more general sampling strategy will not be discussed further.

B. Tomography of vector functions

In this section, consider a vector function $\boldsymbol{g}(x, y, z)$, representing in this particular case the electric or magnetic field probed by proton radiography. Tomographic projections of this function are taken using the (q, s, t), rather than the (x, y, z), components—i.e., the components measured rotate with the angle of probing rather than being fixed in the background coordinate system.

Proton radiography measures electromagnetic field components transverse to the probe direction, so may be understood as a *transverse vector tomography* measurement. By this scheme the s and t components of a vector field are measured. These are given by

$$\begin{aligned} F_\theta^s(s,t) &= \int_{-\infty}^{\infty} \hat{s} \cdot \boldsymbol{g}(x(q,s), y(q,s), t)q \\ &= \int_{-\infty}^{\infty} [g_x(x(q,s), y(q,s), t)\cos\theta \\ &\quad + g_y(x(q,s), y(q,s), t)\sin\theta]q, \end{aligned} \tag{4}$$

$$\begin{aligned} F_\theta^t(s,t) &= \int_{-\infty}^{\infty} \hat{t} \cdot \boldsymbol{g}(x(q,s), y(q,s), t)q \\ &= \int_{-\infty}^{\infty} g_z(x(q,s), y(q,s), t)q. \end{aligned} \tag{5}$$

Tomographic reconstruction using the s component is only able to recover the irrotational part of the field in the x-y plane (i.e., that part of the field whose curl has zero z component).

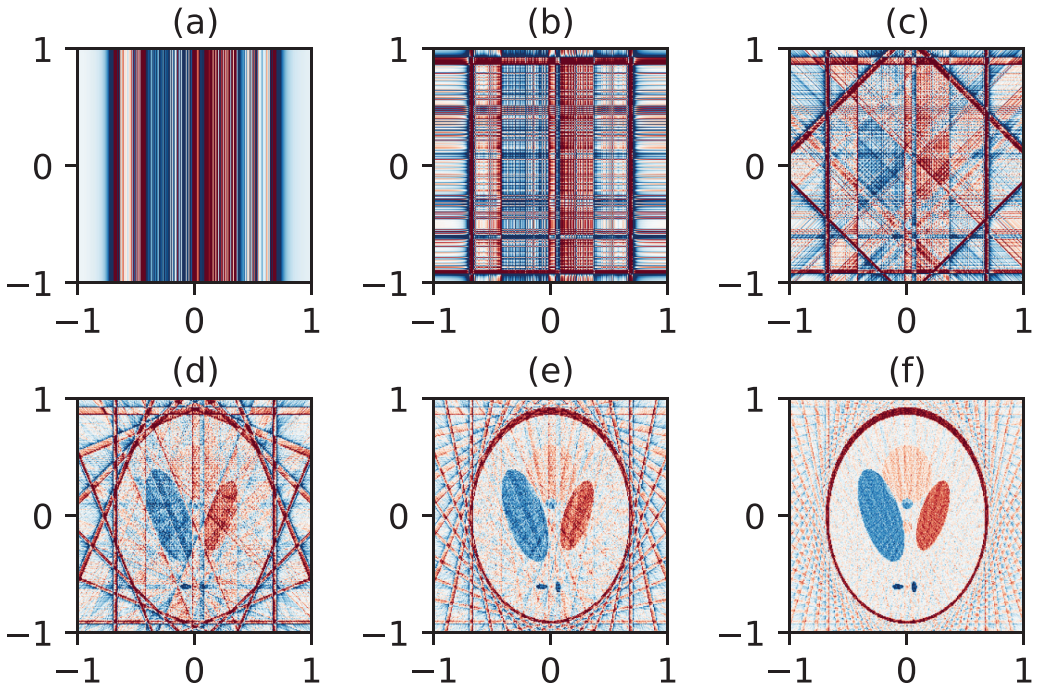

FIG. 3. Example of the failure mode of FBP; 1, 2, 4, 8, 16, and 32 projections are used to produce these images. Linear streaking dominates the reconstruction for $N \leqslant 4$ in (a), (b), and (c). Even for $N > 8$, while the original function is discernible, the exterior of the image continues to show a chequerboard-like pattern. Reconstruction quality, calculated using the structural similarity index metric (SSIM) increases from 5.64% for $N = 1$ view reconstruction in (a) to 35.0% for $N = 32$ in (f).

This can be understood by following similar reasoning to that of [35] for longitudinal vector tomography. This limitation is problematic when considering magnetic fields—the part of the field sourced by currents parallel to the axis of rotation t (or equivalently z in laboratory coordinates) is undetectable, which can be seen from the relevant component of Ampère's Law:

$$\mu_0 J_z = \frac{\partial B_y}{\partial x} - \frac{\partial B_x}{\partial y} = 0. \tag{6}$$

In contrast, because the unit vector $\hat{t} = \hat{z}$ parallel to the axis of rotation is invariant under the rotation which defines the probe geometry, the corresponding component $g_t = g_z$ transforms as a scalar under the rotation and is therefore accessible in full to scalar tomography techniques: Note that the forms of Eqs. (3) and (5) are identical. This justifies only considering methods which involve probe directions constrained to a common plane (as these are the only probe directions which measure field components parallel to the normal vector to that plane), as opposed to those considered by [27] which are beneficial in cases of fixed, nonplanar probe geometry.

The following analysis will therefore focus on this out-of-plane component of the magnetic field—by probing in directions orthogonal to a chosen "rotation" axis, the component parallel to that axis is recoverable. Probing relative to three orthogonal "rotation" axes is therefore sufficient to recover all components of the full three-dimensional vector field. This protocol reduces the problem of three-dimensional transverse vector tomography to a series of two-dimensional scalar tomography problems, allowing the use of well-developed algorithms and numerical techniques from this field, such as the filtered back-projection algorithm.

C. Filtered back-projection

A canonical algorithm for the recovery of tomographic data sets is the *filtered back-projection* (FBP) method [36]. In short, this method filters each projection with a kernel proportional to $|k|$ in Fourier space, then "smears" the filtered projections across their probe directions, summing the resulting "back-projected" functions to recover an approximation of the original function. Formally,

$$f(x, y) \approx \frac{\Delta\theta}{2\pi} \sum_{n=0}^{N-1} G_{\theta_n}(s(x, y, \theta_n)), \tag{7}$$

$$\mathcal{F}_1[G_\theta(s)] = |k| \mathcal{F}_1[F_\theta(s)], \tag{8}$$

where $s(x, y, \theta) = y \cos\theta - x \sin\theta$ as per Eq. (1), and $\mathcal{F}_1$ represents the one-dimensional Fourier transform.

FBP converges to an analytically correct result in the limit of many projections (and can be derived as a discretization of the Fourier projection-slice theorem discussed in Sec. IV), but where samples are few and sparse in the angular dimension it suffers from severe "streaking" artifacts. This behavior is demonstrated in Fig. 3. The quality of reconstructions is quantified using the strucural similarity index metric (SSIM), a popular measure of image similarity, between the input and reconstructed functions [37].

As discussed in the previous section, filtered back-projection is applicable to reconstruction of magnetic fields when applied to the field component parallel to the axis of rotation. The data input to a tomographic reconstruction of a magnetic field measured by proton radiography is shown in Fig. 4. This work employs TomoPy [38] as a back-end for computation of projections and of filtered back-projections.

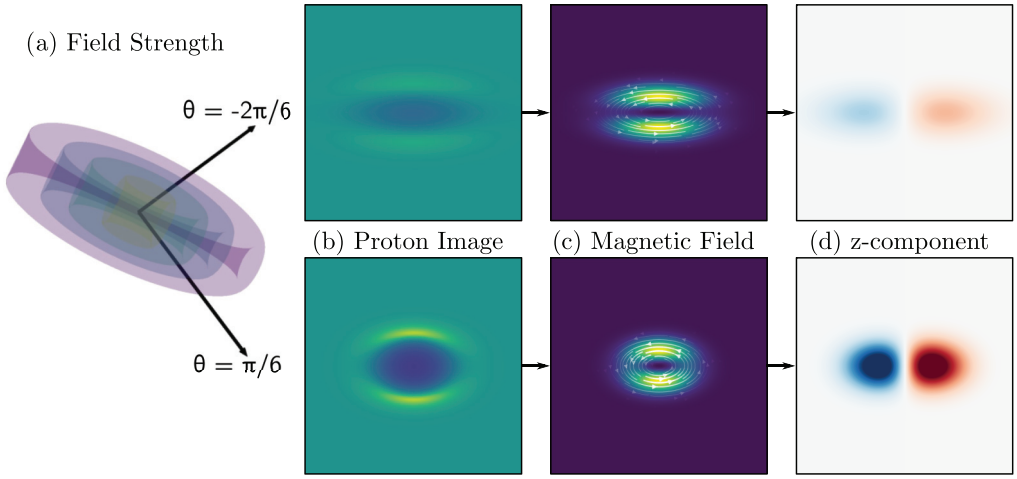

FIG. 4. The different forms of data involved in applying tomographic techniques to proton radiographic data. (a) A three-dimensional rendering of a Gaussian "cocoon" of magnetic field longer in its longitudinal direction than it is transverse. Arrows represent the probe directions shown subsequently. (b) Simulated proton radiographs taken at $\pi/6$ and $-2\pi/6$ from the longitudinal axis. (c) Corresponding line-integrated transverse magnetic field components for each direction. (d) The magnetic field component in each case which is parallel to the "common direction" z. This component is the quantity input to a tomography algorithm such as fitered back-projection, analogous to x-ray attenuation data in x-ray computed tomography.

IV. FOURIER MODE INTERPOLATION

The Fourier projection-slice theorem states that the one-dimensional Fourier transform $\tilde{F}_\theta(k_s)$ of the projection $F_\theta(s)$ is equal to the two-dimensional Fourier transform $\tilde{f}(k_x, k_y)$ of the original function $f(x, y)$, evaluated on a one-dimensional slice through the origin of frequency space normal to the probe direction:

$$\tilde{F}_\theta(k) = \tilde{f}(-k\sin\theta, k\cos\theta). \tag{9}$$

Promoting the parameter θ to a variable, it is clear that $\tilde{F}(k, \theta)$ is in fact nothing more than a representation of $\tilde{f}$ in plane-polar coordinates, albeit with θ differing from the conventional polar angle variable by a quarter-cycle,

$$\tilde{F}(k, \theta - \pi/2) = \tilde{f}(k\cos\theta, k\sin\theta). \tag{10}$$

All that is in principle required for reconstruction of tomographic data is therefore a two-dimensional inverse Fourier transform of the one-dimensional Fourier transforms of projected data. This procedure is analytically exact, but complications arise due to the discrete sampling of real data. How should the inverse Fourier transform of data sampled discretely on a polar grid be computed?

A natural decomposition for data sampled in cylindrical coodinates is the cylindrical harmonics, i.e., a Fourier series in the angular variable θ. This basis set is used by [29] to improve tomographic reconstructions. We propose that data should be collected using probe directions with constant angular separation, $\theta_n = n\pi/N$ for $0 \leqslant n < N$, to allow this Fourier series to be computed using the fast Fourier transform instead of the relatively costly least-squares fitting to Fourier modes involved in the aforementioned publication.

It is easily verified that the the mth angular mode of the real-space function corresponds to the mth angular mode of its Fourier transform and is independent of all other modes, that is:

$$\mathcal{F}_2[f_m(r)e^{-im\theta}] = \tilde{f}_m(k)e^{-im\phi}. \tag{11}$$

Following the work of [39], the relation between each of these angular modes and their Fourier transform is given by the Hankel transform of integer order matching that of the angular mode (the zero-order form of this result is equivalent to the inverse Abel transform). This relationship is as follows:

$$f_m(r) = \frac{i^m}{2\pi}\mathcal{H}_m[\tilde{F}_m(k)]. \tag{12}$$

Higgins and Munson [40] present a direct algorithm for evaluation of the integer-order Hankel transforms involved, but this work takes a different approach—their algorithm is equivalent to the expression for filtered back-projection [Eq. (7)] in the limit where the discrete sum in FBP becomes an integral over angle (high sampling rate) and the angular dependence of the integrand or summand is given by $\exp(-im\phi)$ (an angular Fourier mode).

Therefore, the method of Higgins and Munson may be approximated for any angular mode by passing a filtered back-projection algorithm a set of "virtual projections" with the desired angular dependence, sampled with arbitrary angular density. The result of applying FBP to the virtual projections of each mode is a reconstruction of the corresponding Fourier series component of the original, real-space function f_m, including the $\exp(-im\theta)$ angular dependence.

By linearity of the operations involved, resolving the Fourier series commutes with the FBP operation $\tilde{\mathcal{R}}^{-1}$:

$$f(x, y) \approx \sum_{m=-M}^{M} \tilde{\mathcal{R}}^{-1}[F_m(k)e^{-im\phi}]. \tag{13}$$

$$= \tilde{\mathcal{R}}^{-1}\left[\sum_{m=-M}^{M} F_m(k)e^{-im\phi}\right]$$

$$= \tilde{\mathcal{R}}^{-1}[\hat{F}(k, \phi)]. \tag{14}$$

This equation provides a useful interpretation of $\hat{F}$: It is a version of F "enhanced" by interpolation in ϕ using its Fourier series. This Fourier series agrees with the original

samples F at the sampled angles and is "optimal" in the sense that it is C^∞-smooth and explicitly possesses the same 2π-periodicity that the true function must exhibit.

This procedure can therefore be interpreted simply as an interpolation of the observed projections which enhances the observed data set by filling in between observations without changing the angular Fourier series of the data, and will therefore be termed *Fourier interpolation*.

The procedure proposed here has some advantages over the one used by [29], especially when data are sampled uniformly in angle as suggested above.

First, where data are sampled uniformly the interpolation can be carried out using an FFT, padding in Fourier space, and an inverse FFT; when nonuniform sampling is necessary it can be performed using standard trigonometric interpolation formulas [41]. Either of these options should outperform the solution of a linear system required by [29], though for small numbers of projections the difference in computation time is not expected to be significant.

The complexity of implementing the method is also reduced, as existing implementations of filtered back-projection can be used to compute the Hankel transforms rather than computing them individually for each different angular mode.

Finally, the interpretation of the resulting algorithm as the application of a standard tomographic reconstruction algorithm to data enhanced using Fourier-series interpolation implies that algorithms other than FBP could be used to implement that stage of the process. This provides a natural route to incorporation as a "preprocessing" step in, for example, iterative, algebraic reconstruction techniques which are able to use *a priori* knowledge about the function under observation to improve the quality of reconstruction [36].

Demonstration of Fourier-interpolated tomographic reconstruction

Figure 3 was recreated using the Fourier interpolation technique to pre-enhance the set of all projections. The result is shown in Fig. 5. It can be seen that in all cases the properties of the interpolated reconstruction are improved versus the noninterpolated. For example, while the naïve application of filtered back-projection in Fig. 3 results in functions featuring streaks that reach the edges of the image (and would continue arbitrarily far if the reconstruction was carried out on a larger domain), the reconstruction of Fourier-interpolated images is compactly supported on the smallest disk that completely contains the support of the original function. Effectively, the linear streaks seen in the FBP reconstructions correspond to circular streaks of constant radius in the reconstructed image, and these circular streaks will—for many functions—represent less of a deviation from the original function than the linear streaks characteristic of FBP in the sparse sampling regime. This correspondence reflects the relationship between standard FBP and the polar-coordinates approach taken in the derivation of this method: Artifacts in FBP arise from "smearing" the observations along the direction of observation; artifacts in Fourier-interpolated FBP represent a "smearing" in the polar angle.

Further, the most noticeable artifacts in, for example, the reconstruction of Fig. 5(c) appear in the region where the elliptical support of the original function does not fill the circular support of the reconstruction. This indicates that the reconstruction may be improved further by employing a virtual transformation to the computational domain of the algorithm to ensure the best possible overlap between the original function's region of support and the disk containing that region. In the next section, this conjecture is investigated and a method is derived to achieve the necessary transformation.

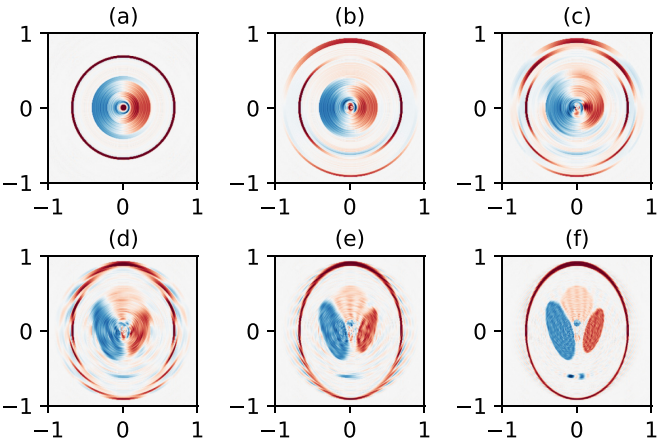

FIG. 5. Demonstration of the improvement attainable by using Fourier interpolation techniques. Images were produced identically to Fig. 3, except that the set of projections was enhanced by interpolation to an angular frequency of 1024 view angles prior to reconstruction. Noise and streaking are significantly reduced, though performance is still quite poor for very small numbers of projections. Linear streaking has been replaced by circular streaking, reflecting this method's polar-coordinates formulation as opposed to the Cartesian formulation of standard FBP. SSIM reconstruction quality increases from 74.6% ($N = 1$) in (a) to 85.9% ($N = 32$) in (f).

V. ASPECT RATIO COMPENSATION: ELLIPTICAL TOMOGRAPHY

Many realistic functions are not best described as being supported on a disk but have some aspect ratio not equal to unity. These functions, represented by their projections as a sinogram, have a width that oscillates with angle, an effect seen for example in the right panel of Fig. 2. Altering the procedure used such that the object appears to have aspect ratio closer to unity may be expected to improve the reconstruction quality. This may be achieved by applying a uniaxial scaling between the physical and computational domains of the problem. There are three things which must be considered when implementing such a scaling: First, the angular separation of observations in physical space becomes nonuniform in order to maintain uniform angular sampling in computational space; second, an individual scaling of the s axis must be applied to projections, accounting for the stretching or shrinking of the axis perpendicular to the projection; and, third, this must be compensated for using an inverse scaling of the function values to maintain equality of all projections' integrals along s.

As an example, the modified Shepp-Logan phantom used in Figs. 3 and 5 is defined on the two-dimensional domain $[-1, 1] \times [-1, 1]$ and composed of several ellipses with

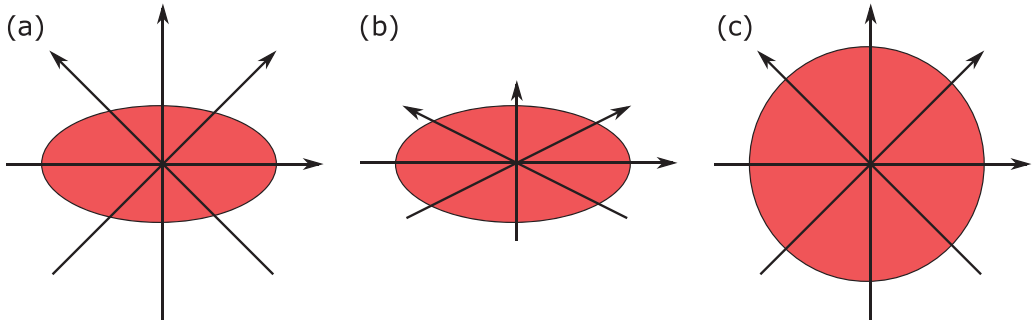

FIG. 6. Schematic depiction of the aspect ratio compensation method for an elliptical target function of aspect ratio 2:1. (a) Uniform sampling of the elliptical target function by four probes. (b) Sampling at angles given by Equation 16 for a compensation ratio of 2:1, showing nonuniform sampling in the physical domain. (c) Transformation into the computational domain of panel (b), showing that in the computational domain sampling is uniform in angle and the target has been transformed into a circle.

differing parameters. The support of this function is defined by the largest ellipse, which entirely contains all other ellipses and has minor and major semiaxis lengths in the ratio $A = 3:4$. We now detail the procedure for tomography of this phantom using aspect ratio compensation between the physical domain with coordinates $(X, Y; R, \Theta)$ and the computational domain with coordinates $(x, y; r, \theta)$.

The relation between Cartesian coordinates is such as to equalize the aspect ratio of the function under observation. Keeping $x = X$, this implies $y = Y/A$. Angles of projection are uniformly spaced in the computational domain:

$$\theta_k = \frac{k\pi}{N} \quad (0 \leqslant k < N). \tag{15}$$

Using the relationship between Cartesian coordinates, it is easy to derive the corresponding relationship for the angular variables Θ and θ:

$$\tan\Theta = \frac{Y}{X} = \frac{Ay}{x} = A\tan\theta. \tag{16}$$

This has the effect of reducing angular spacing when the probe direction is close to the major axis and increasing angular spacing when close to the minor axis and is demonstrated in Fig. 6.

The transverse extent of the physical-space object varies with viewing angle, and this must also be compensated for. The physical transverse width of the ellipse is

$$\begin{aligned} w(\Theta) &= \sqrt{w_{\max}^2\cos^2\Theta + w_{\min}^2\sin^2\Theta} \\ &= w_{\max}\cos\Theta\sqrt{1 + A^{-2}\tan^2\Theta} \\ &= w_{\max}\cos\Theta\sqrt{1 + \tan^2\theta} \\ &= w_{\max}\frac{\cos\Theta}{\cos\theta}. \end{aligned} \tag{17}$$

The s axis of each projection is rescaled by a factor $w(\Theta)/w_{\min} = A\cos\Theta/\cos\theta$ to account for the transverse stretching caused by aspect ratio correction, and the magnitudes of each projection's values are scaled by the inverse value [Equation (17) is used preferentially as the limit $\Theta = \theta = \pi/2$ is not problematic in this form]. This has the effect of eliminating the oscillation of the sinogram's width as a function of Θ. The techniques detailed above in Sec. III may then be applied to this modified sinogram and the end result of the reconstruction is stretched to reintroduce the physically correct aspect ratio. The result of this procedure is shown in Fig. 7.

VI. APPLICATIONS

We now turn our attention to the important example of imaging laser-plasma interactions with very large aspect ratios, such as channelling processes [16], jets in laboratory plasma astrophysics experiments [42], and z-pinches [43]. To demonstrate its utility for the first of these applications, magnetic fields have been extracted from a particle-in-cell simulation of a high-intensity laser pulse propagating into a plasma with a preformed density gradient. The laser pulse carried 500 J in 500 fs at a wavelength of 1 μm and was focused to a vacuum focal spot diameter of 10 μm. It propagated into a plasma of density gradient 500 μm up to approximately critical density, where its energy was absorbed by the plasma. A representation of the resulting magnetic fields is shown in Fig. 8; by this point in the simulation residual electric fields had decayed to be insignificant in comparison to the magnetic fields, which are of the order of 1 kT in magnitude.

The results of reconstructing this field structure with and without both Fourier interpolation and 10:1 aspect ratio compensation are shown in Fig. 8. The performance of each enhancement technique presented here, separately and in combination, is plotted as a function of the number of probe views available, and an example reconstruction is displayed for eleven views. It is notable that achieving a SSIM reconstruction quality of 90% requires nearly sixty probes when FBP is used without our enhancement techniques, but when both are combined only five probes are needed to attain this level of quality. The highly elongated nature of the field displayed in Fig. 8 causes severe problems in the absence of aspect ratio compensation, though Fourier-series interpolation improves the appearance of the final result. Even with aspect-ratio compensation applied, without Fourier interpolation the result still suffers from streaking artifacts which can obscure the true field. At all sampling rates tested, applying both techniques together performs significantly better than either individually, demonstrating that the noise- and artifact-reduction properties of Fourier-series interpolation complement the more efficient sampling facilitated by aspect ratio compensation.

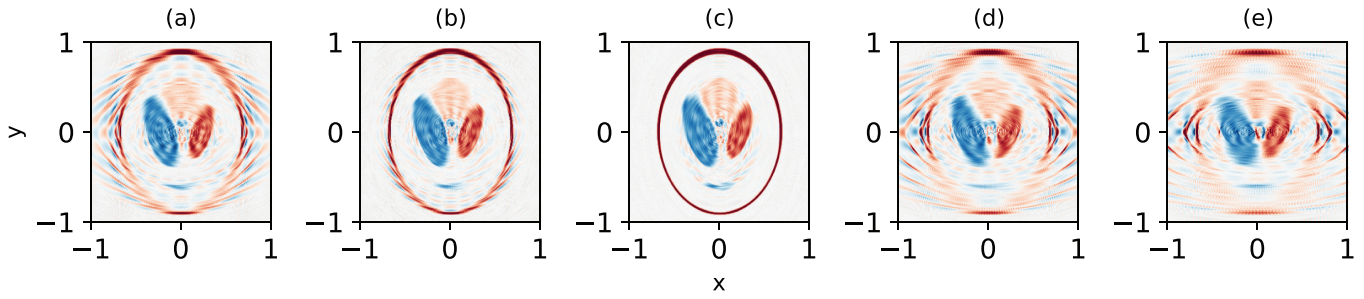

FIG. 7. The effect of aspect ratio compensation on reconstruction quality. All reconstructions were carried out using 15 projections, and expected aspect ratios of (a) 4:3 (SSIM: 47.5%), (b) 1:1 (SSIM: 69.0%), (c) 3:4 (SSIM: 87.2%), (d) 9:16 (SSIM: 39.5%), and (e) 27:64 (SSIM: 35.3%) chosen as they are integer powers of the correct 3:4 ratio. (b) No compensation; (c) the correct level of compensation and resultantly the highest quality of reconstruction; (a) the correct ratio but in the wrong direction, worsening the quality of the reconstruction; [(d) and (e)] "squeeze" the function due to excessive compensation. It is clear that compensation for aspect ratio can improve reconstruction quality if applied appropriately.

Experimental implementation

The above discussion has shown that a relatively small number of probe directions—on the order of 10—is sufficient to produce good-quality reconstructions of even very elongated magnetic field structures. We now address the issue of experimentally implementing the methods of proton tomography derived above in experiments, in particular how to increase the limited number of proton radiography probe directions which can be run simultaneously.

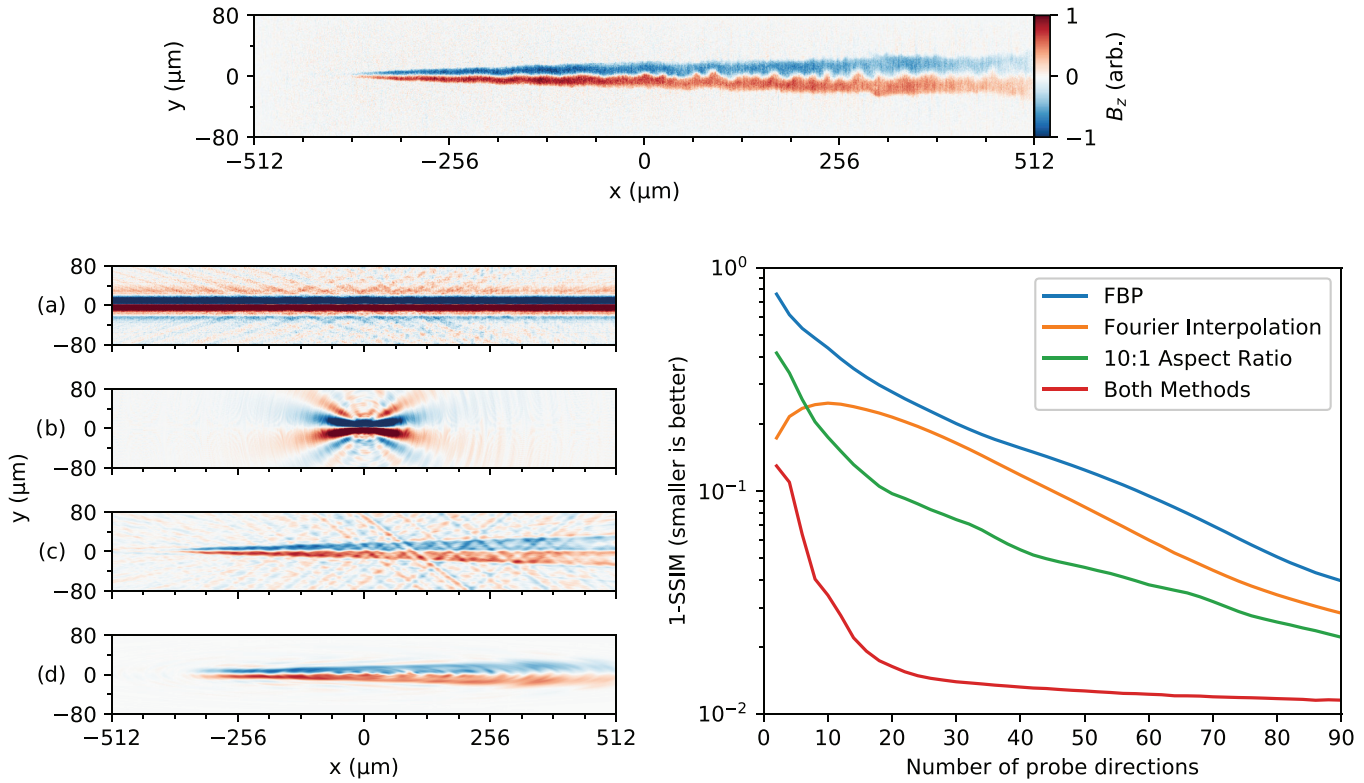

FIG. 8. Above: Z-component of magnetic field extracted from a particle-in-cell simulation of a laser-plasma channelling interaction, approximately kT in magnitude. The field is shown in two dimensions, averaged over the z axis of the simulation to improve legibility. All of the methods presented here are however applicable to three-dimensional data sets as well as two-dimensional ones. Below left: Reconstructions produced using a sampling rate $N = 11$ views. (a) presents the results of applying naïve filtered back-projection, (b) includes aspect ratio-compensation, (c) includes Fourier-series interpolation and (d) includes both. Aspect ratio compensation uses a ratio of 10:1. Below right: Quantitative image reconstruction quality [37], plotted as $1 - \texttt{SSIM}$ such that smaller values are better, with 0 representing perfect reconstruction. While each technique struggles with this field when used individually, the composition of both techniques produces results of good quality even for very sparse sampling, equivalent to FBP using numbers of views orders of magnitude larger: Ninety percent SSIM is achieved for five view angles when both enhancements are applied; without them this quality level requires 58. All reconstructions are plotted using the same color scaling as the original field.

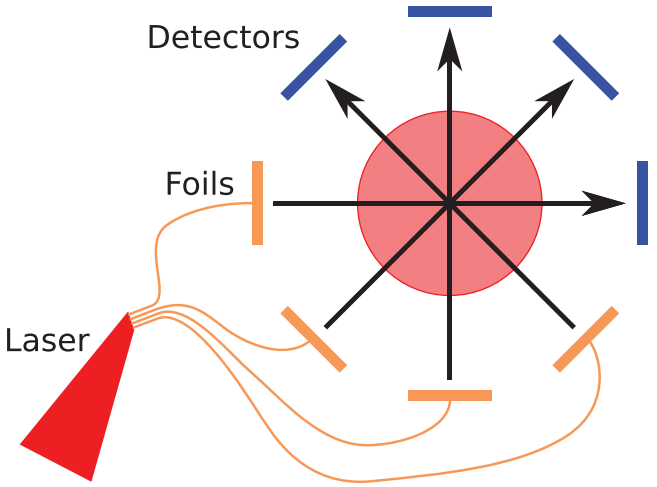

FIG. 9. Simplified schematic of the proposed scheme, used to probe a single target with four proton beams. The use of multiple short pulses would enable more proton beams to be driven simultaneously, but for simplicity this schematic only shows one short pulse driving a bundle of four beam foils.

When proton beams are driven by the target normal sheath acceleration (TNSA) mechanism [44] one high-energy short pulse is required per beam, and the number of short pulses available at existing facilities is very limited, with many (for example, the United Kingdom's Orion and Vulcan [45] and OMEGA EP [46] in the United States) providing two short pulses. The National Ignition Facility's Advanced Radiographic Capability system has been demonstrated with four independent beamlets [47,48] and is designed to eventually provide eight [49,50]. Thus, even numbers of projections considered "very sparse" by the wider computed tomography community (75 in Ref. [51]) are far larger than the number of beams producible via TNSA on a single shot.

Experiments at long-pulse facilities have used an exploding-pusher implosion capsule system to produce proton beams [32]. As these capsules are driven by long pulses this provides hope for scaling to larger numbers of capsules at facilities with many long pulses, such as the NIF, OMEGA, and Laser Mégajoule. However, the isotropic nature of the proton production by these sources implies a poor efficiency of conversion from laser energy into the section of the beam which probes the target, and may also present shielding and crosstalk issues if several capsules are imploded simultaneously.

We present a third option which resembles the target configuration used to produce TNSA protons. The proposed scheme consists of several metal (in the simulations presented, gold) foils connected to conductive wires. The foils are located at arbitrary points in space according to the desired probe geometry, and the conductive wires connected to their rear faces are bundled together. A schematic representation of this geometry is shown in Fig. 9. When a laser pulse is incident on the bundled ends of the wires, electrons are expelled and a space-charge imbalance is set up in and around the wire ends. This outflow of electrons is balanced by large return currents along the wires' surfaces. These currents ultimately lead to positive charging of the secondary foils, expelling the relatively light hydrogen ions while the gold ions respond more slowly.

This experimental configuration has been tested in particle-in-cell simulations using the code `Smilei` [52]. The test version of the geometry shown in Fig. 10 includes only two beam-producing foils and much shorter wires than would be used in an experiment in order to reduce the computational cost of the simulations to an acceptable level. The spectrum of ions produced by this new acceleration geometry is compared to a more conventional TNSA geometry (for comparable laser and target parameters) in Fig. 10, showing that these ions are also suitable for imaging plasma electromagnetic fields.

VII. SUMMARY AND CONCLUSIONS

Proton radiography has found many applications for probing magnetic field structures in plasma. However, its extension to three dimensional reconstruction remains a significant challenge. To this end, two preprocessing techniques for improving the performance of a standard tomographic reconstruction algorithm—filtered back-projection—have been explored in this article.

First, Fourier decomposition of observations in the angular parameter was proposed as a method for inversion of the Radon transform, derived from manipulation of the Fourier projection-slice theorem. By approximating the calculation of the general integer-order Hankel transform using back-projection, a single filtered back-projection of interpolated data is able to replace the calculation of a different integer-order Hankel transform per angular mode, greatly reducing the computational complexity of the method.

Second, based on the properties of Fourier-interpolated reconstructions, this method of tomography has been shown to achieve better accuracy for small numbers of observations when the aspect ratio of the function being observed is close to unity. To benefit from this observation, relations linking physical space and a computational space which differ by a nonuniform scaling have been derived, and these relations allow aspect ratios far from unity to be compensated for. The effectiveness of this compensation technique has been demonstrated using a modified Shepp-Logan phantom, which is supported on an ellipse of aspect ratio 3:4.

The effectiveness of these new proposed preprocessing enhancement steps, both individually and in combination has been compared to unmodified filtered back-projection. It has been shown that in the case of the magnetic field of a simulated laser channel in dense plasma, each new preprocessing method improves the quality of reconstruction, and that combining them produces the best results of all. This significantly improves the prospects of a tomographic approach to proton radiography being implemented.

Finally, a novel experimental geometry for accelerating proton beams has been presented, and is proposed to enable the generation of several proton beams from each available short pulse, further improving the possibility of useful apppplication of tomographic concepts to proton radiography.

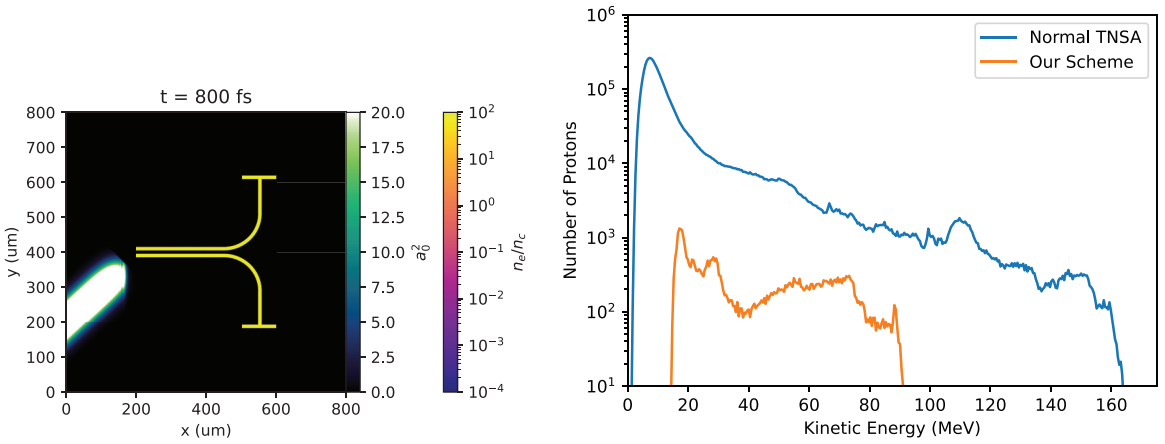

FIG. 10. Particle-in-cell simulation set-up for the proposed novel acceleration geometry. A 2 ps, $a_0 = 10$ laser pulse is about to impinge on solid-density metal wires, driving surface currents which lead to proton acceleration from the foils at the wires' ends. The spectrum of the protons accelerated by this interaction is compared to those produced by TNSA using the same laser parameters and target material and is proposed to be suitable for radiographic applications based on this.

ACKNOWLEDGMENTS

The authors gratefully acknowledge the support of all the staff at the Central Laser Facility, UKRI-STFC Rutherford Appleton Laboratory and the ORION Laser Facilty at AWE Aldermaston (particularly discussions with Gavin Crow) while undertaking this research. This work has been carried out within the framework of the EUROfusion Consortium and has received funding from the Euratom research and training programme 2014-2018 and 2019-2020 under Grant Agreement No. 633053. The views and opinions expressed herein do not necessarily reflect those of the European Commission. We also acknowledge the support of STFC Grants No. ST/P002048/1 and No. ST/V001655/1, along with EPSRC Grants No. EP/R029148/1 and No. EP/L000237/1. B.T.S. acknowledges support from UKRI-EPSRC under iCASE studentship 1950656 (in association with AWE plc). P.A.N. acknowledges support from OxCHEDS for his William Penney Fellowship. The simulations presented herein were carried out using the ARCHER2 UK National Supercomputing Service (EPSRC project e674).

[1] M. Borghesi, A. Schiavi, D. H. Campbell, M. G. Haines, O. Willi, A. J. MacKinnon, L. A. Gizzi, M. Galimberti, R. J. Clarke, and H. Ruhl, Proton imaging: A diagnostic for inertial confinement fusion/fast ignitor studies, Plasma Phys. Control. Fus. **43**, A267 (2001).

[2] A. J. Mackinnon, P. K. Patel, R. P. Town, M. J. Edwards, T. Phillips, S. C. Lerner, D. W. Price, D. Hicks, M. H. Key, S. Hatchett, S. C. Wilks, M. Borghesi, L. Romagnani, S. Kar, T. Toncian, G. Pretzler, O. Willi, M. Koenig, E. Martinolli, S. Lepape *et al.*, Proton radiography as an electromagnetic field and density perturbation diagnostic (invited), Rev. Sci. Instrum. **75**, 3531 (2004).

[3] N. L. Kugland, J. S. Ross, P.-Y. Chang, R. P. Drake, G. Fiksel, D. H. Froula, S. H. Glenzer, G. Gregori, M. Grosskopf, C. Huntington, M. Koenig, Y. Kuramitsu, C. Kuranz, M. C. Levy, E. Liang, D. Martinez, J. Meinecke, F. Miniati, T. Morita, A. Pelka *et al.*, Visualizing electromagnetic fields in laser-produced counter-streaming plasma experiments for collisionless shock laboratory astrophysics, Phys. Plasmas **20**, 056313 (2013).

[4] T. Morita, N. L. Kugland, W. Wan, R. Crowston, R. P. Drake, F. Fiuza, G. Gregori, C. Huntington, T. Ishikawa, M. Koenig, C. Kuranz, M. C. Levy, D. Martinez, J. Meinecke, F. Miniati, C. D. Murphy, A. Pelka, C. Plechaty, R. Presura, N. Quirós *et al.*, Proton imaging of an electrostatic field structure formed in laser-produced counter-streaming plasmas, J. Phys.: Conf. Ser. **688**, 012071 (2016).

[5] H.-S. Park, J. S. Ross, C. M. Huntington, F. Fiuza, D. Ryutov, D. Casey, R. P. Drake, G. Fiksel, D. Froula, G. Gregori, N. L. Kugland, C. Kuranz, M. C. Levy, C. K. Li, J. Meinecke, T. Morita, R. Petrasso, C. Plechaty, B. Remington, Y. Sakawa *et al.*, Laboratory astrophysical collisionless shock experiments on Omega and NIF, J. Phys.: Conf. Ser. **688**, 012084 (2016).

[6] C. M. Huntington, M. J.-E. Manuel, J. S. Ross, S. C. Wilks, F. Fiuza, H. G. Rinderknecht, H.-S. Park, G. Gregori, D. P. Higginson, J. Park, B. B. Pollock, B. A. Remington, D. D. Ryutov, C. Ruyer, Y. Sakawa, H. Sio, A. Spitkovsky, G. F. Swadling, H. Takabe, and A. B. Zylstra, Magnetic field production via the Weibel instability in interpenetrating plasma flows, Phys. Plasmas **24**, 041410 (2017).

[7] P. Tzeferacos, A. Rigby, A. F. A. Bott, A. R. Bell, R. Bingham, A. Casner, F. Cattaneo, E. M. Churazov, J. Emig, F. Fiuza, C. B. Forest, J. Foster, C. Graziani, J. Katz, M. Koenig, C.-K. Li, J. Meinecke, R. Petrasso, H.-S. Park, B. A. Remington *et al.*, Laboratory evidence of dynamo amplification of magnetic fields in a turbulent plasma, Nat. Commun. **9**, 591 (2018).

[8] C. A. J. Palmer, P. T. Campbell, Y. Ma, L. Antonelli, A. F. A. Bott, G. Gregori, J. Halliday, Y. Katzir, P. Kordell, K. Krushelnick, S. V. Lebedev, E. Montgomery, M. Notley, D. C. Carroll, C. P. Ridgers, A. A. Schekochihin, M. J. V. Streeter, A. G. R. Thomas, E. R. Tubman, N. Woolsey *et al.*, Field reconstruction from proton radiography of intense laser driven magnetic reconnection, Phys. Plasmas **26**, 083109 (2019).

[9] E. R. Tubman, A. S. Joglekar, A. F. A. Bott, M. Borghesi, B. Coleman, G. Cooper, C. N. Danson, P. Durey, J. M. Foster, P. Graham, G. Gregori, E. T. Gumbrell, M. P. Hill, T. Hodge, S. Kar, R. J. Kingham, M. Read, C. P. Ridgers, J. Skidmore, C. Spindloe *et al.*, Observations of pressure anisotropy effects within semi-collisional magnetized plasma bubbles, Nat. Commun. **12**, 334 (2021).

[10] J. R. Rygg, F. H. Séguin, C. K. Li, J. A. Frenje, M. J.-E. Manuel, R. D. Petrasso, R. Betti, J. A. Delettrez, O. V. Gotchev, J. P. Knauer, D. D. Meyerhofer, F. J. Marshall, C. Stoeckl, and W. Theobald, Proton radiography of inertial fusion implosions, Science **319**, 1223 (2008).

[11] C. K. Li, F. H. Séguin, J. A. Frenje, M. Manuel, D. Casey, N. Sinenian, R. D. Petrasso, P. A. Amendt, O. L. Landen, J. R. Rygg, R. P. J. Town, R. Betti, J. Delettrez, J. P. Knauer, F. Marshall, D. D. Meyerhofer, T. C. Sangster, D. Shvarts, V. A. Smalyuk, J. M. Soures *et al.*, Proton radiography of dynamic electric and magnetic fields in laser-produced high-energy-density plasmas, Phys. Plasmas **16**, 056304 (2009).

[12] A. J. Mackinnon, P. K. Patel, M. Borghesi, R. C. Clarke, R. R. Freeman, H. Habara, S. P. Hatchett, D. Hey, D. G. Hicks, S. Kar, M. H. Key, J. A. King, K. Lancaster, D. Neely, A. Nikkro, P. A. Norreys, M. M. Notley, T. W. Phillips, L. Romagnani, R. A. Snavely *et al.*, Proton Radiography of a Laser-Driven Implosion, Phys. Rev. Lett. **97**, 045001 (2006).

[13] G. Sarri, C. A. Cecchetti, L. Romagnani, C. M. Brown, D. J. Hoarty, S. James, J. Morton, M. E. Dieckmann, R. Jung, O. Willi, S. V. Bulanov, F. Pegoraro, and M. Borghesi, The application of laser-driven proton beams to the radiography of intense laser-hohlraum interactions, New J. Phys. **12**, 045006 (2010).

[14] C. K. Li, F. H. Séguin, J. A. Frenje, R. D. Petrasso, P. A. Amendt, R. P. J. Town, O. L. Landen, J. R. Rygg, R. Betti, J. P. Knauer, D. D. Meyerhofer, J. M. Soures, C. A. Back, J. D. Kilkenny, and A. Nikroo, Observations of Electromagnetic Fields and Plasma Flow in Hohlraums with Proton Radiography, Phys. Rev. Lett. **102**, 205001 (2009).

[15] C. K. Li, F. H. Séguin, J. A. Frenje, M. Rosenberg, R. D. Petrasso, P. A. Amendt, J. A. Koch, O. L. Landen, H. S. Park, H. F. Robey, R. P. J. Town, A. Casner, F. Philippe, R. Betti, J. P. Knauer, D. D. Meyerhofer, C. A. Back, J. D. Kilkenny, and A. Nikroo, Charged-particle probing of X-ray–Driven inertial-fusion implosions, Science **327**, 1231 (2010).

[16] B. T. Spiers, M. P. Hill, C. Brown, L. Ceurvorst, N. Ratan, A. F. Savin, P. Allan, E. Floyd, J. Fyrth, L. Hobbs, S. James, J. Luis, M. Ramsay, N. Sircombe, J. Skidmore, R. Aboushelbaya, M. W. Mayr, R. Paddock, R. H. W. Wang, and P. A. Norreys, Whole-beam self-focusing in fusion-relevant plasma, Philos. Trans. R. Soc. A **379**, 20200159 (2021).

[17] A. Rigby, J. Katz, A. F. A. Bott, T. G. White, P. Tzeferacos, D. Q. Lamb, D. H. Froula, and G. Gregori, Implementation of a Faraday rotation diagnostic at the OMEGA laser facility, High Power Laser Sci. Eng. **6**, e49 (2018).

[18] A. J. Mackinnon, M. Borghesi, S. Hatchett, M. H. Key, P. K. Patel, H. Campbell, A. Schiavi, R. Snavely, S. C. Wilks, and O. Willi, Effect of Plasma Scale Length on Multi-MeV Proton Production by Intense Laser Pulses, Phys. Rev. Lett. **86**, 1769 (2001).

[19] C. Scullion, D. Doria, L. Romagnani, H. Ahmed, A. Alejo, O. C. Ettlinger, R. J. Gray, J. Green, G. S. Hicks, D. Jung, K. Naughton, H. Padda, K. Poder, G. G. Scott, D. R. Symes, S. Kar, P. McKenna, Z. Najmudin, D. Neely, M. Zepf *et al.*, Angularly resolved characterization of ion beams from laser-ultrathin foil interactions, J. Instrum. **11**, C09020 (2016).

[20] N. L. Kugland, D. D. Ryutov, C. Plechaty, J. S. Ross, and H.-S. Park, Invited article: Relation between electric and magnetic field structures and their proton-beam images, Rev. Sci. Instrum. **83**, 101301 (2012).

[21] M. F. Kasim, L. Ceurvorst, N. Ratan, J. Sadler, N. Chen, A. Sävert, R. Trines, R. Bingham, P. N. Burrows, M. C. Kaluza, and P. Norreys, Quantitative shadowgraphy and proton radiography for large intensity modulations, Phys. Rev. E **95**, 023306 (2017).

[22] A. F. A. Bott, C. Graziani, P. Tzeferacos, T. G. White, D. Q. Lamb, G. Gregori, and A. A. Schekochihin, Proton imaging of stochastic magnetic fields, J. Plasma Phys. **83**, 905830614 (2017).

[23] M. F. Kasim, A. F. A. Bott, P. Tzeferacos, D. Q. Lamb, G. Gregori, and S. M. Vinko, Retrieving fields from proton radiography without source profiles, Phys. Rev. E **100**, 033208 (2019).

[24] N. F. Y. Chen, M. F. Kasim, L. Ceurvorst, N. Ratan, J. Sadler, M. C. Levy, R. Trines, R. Bingham, and P. Norreys, Machine learning applied to proton radiography of high-energy-density plasmas, Phys. Rev. E **95**, 043305 (2017).

[25] C. K. Li, F. H. Séguin, J. A. Frenje, J. R. Rygg, R. D. Petrasso, R. P. J. Town, P. A. Amendt, S. P. Hatchett, O. L. Landen, A. J. Mackinnon, P. K. Patel, V. A. Smalyuk, T. C. Sangster, and J. P. Knauer, Measuring E and B Fields in Laser-Produced Plasmas with Monoenergetic Proton Radiography, Phys. Rev. Lett. **97**, 135003 (2006).

[26] P. L. Volegov, C. R. Danly, F. E. Merrill, R. Simpson, and C. H. Wilde, On three-dimensional reconstruction of a neutron/x-ray source from very few two-dimensional projections, J. Appl. Phys. **118**, 205903 (2015).

[27] P. L. Volegov, C. R. Danly, D. Fittinghoff, V. Geppert-Kleinrath, G. Grim, F. E. Merrill, and C. H. Wilde, Three-dimensional reconstruction of neutron, gamma-ray, and x-ray sources using spherical harmonic decomposition, J. Appl. Phys. **122**, 175901 (2017).

[28] P. L. Volegov, S. H. Batha, V. Geppert-Kleinrath, C. R. Danly, F. E. Merrill, C. H. Wilde, D. C. Wilson, D. T. Casey, D. Fittinghoff, B. Appelbe, J. P. Chittenden, A. J. Crilly, and K. McGlinchey, Density determination of the thermonuclear fuel region in inertial confinement fusion implosions, J. Appl. Phys. **127**, 083301 (2020).

[29] P. L. Volegov, S. H. Batha, D. N. Fittinghoff, C. R. Danly, V. Geppert-Kleinrath, C. H. Wilde, and A. B. Zylstra, Three-dimensional reconstruction of neutron, gamma-ray, and x-ray sources using a cylindrical-harmonics expansion, Rev. Sci. Instrum. **92**, 033508 (2021).

[30] A. G. Smyth, G. Sarri, M. Vranic, Y. Amano, D. Doria, E. Guillaume, H. Habara, R. Heathcote, G. Hicks, Z. Najmudin, H. Nakamura, P. A. Norreys, S. Kar, L. O. Silva, K. A. Tanaka, J. Vieira, and M. Borghesi, Magnetic field generation during intense laser channelling in underdense plasma, Phys. Plasmas **23**, 063121 (2016).

[31] B. Du, H.-B. Cai, W.-S. Zhang, X.-F. Wang, D.-G. Kang, L. Deng, E.-H. Zhang, P.-L. Yao, X.-X. Yan, S.-Y. Zou, and S.-P. Zhu, Separating the contributions of electric and magnetic fields in deflecting the probes in proton radiography with multiple proton energies, Matter Radiat. Extremes **6**, 035903 (2021).

[32] C. K. Li, F. H. Séguin, J. A. Frenje, J. R. Rygg, R. D. Petrasso, R. P. J. Town, P. A. Amendt, S. P. Hatchett, O. L. Landen, A. J. Mackinnon, P. K. Patel, V. A. Smalyuk, J. P. Knauer, T. C. Sangster, and C. Stoeckl, Monoenergetic proton backlighter for measuring E and B fields and for radiographing implosions and high-energy density plasmas (invited), Rev. Sci. Instrum. **77**, 10E725 (2006).

[33] J. T. Laune, S. Feister, and P. Tzeferacos, PROBLEM: PROton-imaged B-field nonLinear Extraction Module (2021), https://github.com/flash-center/PROBLEM.

[34] L. A. Shepp and B. F. Logan, The Fourier reconstruction of a head section, IEEE Trans. Nucl. Sci. **21**, 21 (1974).

[35] S. J. Norton, Tomographic reconstruction of 2-D vector fields: Application to flow imaging, Geophys. J. Int. **97**, 161 (1989).

[36] D. Dudgeon and R. Mersereau, *Multidimensional Digital Signal Processing* (Prentice-Hall, Hoboken, NJ, 1984).

[37] Z. Wang, A. Bovik, H. Sheikh, and E. Simoncelli, Image quality assessment: From error visibility to structural similarity, IEEE Trans. Image Process. **13**, 600 (2004).

[38] D. Gürsoy, F. De Carlo, X. Xiao, and C. Jacobsen, TomoPy: A framework for the analysis of synchrotron tomographic data, J. Synchrotron Radiat. **21**, 1188 (2014).

[39] W. Higgins and D. Munson, A Hankel transform approach to tomographic image reconstruction, IEEE Trans. Med. Imaging **7**, 59 (1988).

[40] W. Higgins and D. Munson, An algorithm for computing general integer-order Hankel transforms, IEEE Trans. Acoust. Speech Sign. Process. **35**, 86 (1987).

[41] A. Zygmund, Trigonometric interpolation, in *Trigonometric Series*, Cambridge Mathematical Library, 3rd ed. (Cambridge University Press, Cambridge, UK, 2003), pp. 393–450.

[42] C. K. Li, P. Tzeferacos, D. Lamb, G. Gregori, P. A. Norreys, M. J. Rosenberg, R. K. Follett, D. H. Froula, M. Koenig, F. H. Seguin, J. A. Frenje, H. G. Rinderknecht, H. Sio, A. B. Zylstra, R. D. Petrasso, P. A. Amendt, H. S. Park, B. A. Remington, D. D. Ryutov, S. C. Wilks *et al.*, Scaled laboratory experiments explain the kink behaviour of the Crab Nebula jet, Nat. Commun. **7**, 13081 (2016).

[43] S. Lebedev, R. B. Spielman, and X. Li, Editorial for special issue on Z-pinches, Matter Radiat. Extr. **4**, 063001 (2019).

[44] M. Passoni, L. Bertagna, and A. Zani, Target normal sheath acceleration: Theory, comparison with experiments and future perspectives, New J. Phys. **12**, 045012 (2010).

[45] C. Danson, D. Neely, and D. Hillier, Pulse fidelity in ultra-high-power (petawatt class) laser systems, High Power Laser Sci. Eng. **2**, e34 (2014).

[46] D. N. Maywar, J. H. Kelly, L. J. Waxer, S. F. B. Morse, I. A. Begishev, J. Bromage, C. Dorrer, J. L. Edwards, L. Folnsbee, M. J. Guardalben, S. D. Jacobs, R. Jungquist, T. J. Kessler, R. W. Kidder, B. E. Kruschwitz, S. J. Loucks, J. R. Marciante, R. L. McCrory, D. D. Meyerhofer, A. V. Okishev *et al.*, OMEGA EP high-energy petawatt laser: Progress and prospects, J. Phys.: Conf. Ser. **112**, 032007 (2008).

[47] D. Mariscal, T. Ma, S. C. Wilks, A. J. Kemp, G. J. Williams, P. Michel, H. Chen, P. K. Patel, B. A. Remington, M. Bowers, L. Pelz, M. R. Hermann, W. Hsing, D. Martinez, R. Sigurdsson, M. Prantil, A. Conder, J. Lawson, M. Hamamoto, P. Di Nicola *et al.*, First demonstration of ARC-accelerated proton beams at the National Ignition Facility, Phys. Plasmas **26**, 043110 (2019).

[48] W. H. Williams, J. K. Crane, D. A. Alessi, C. D. Boley, M. W. Bowers, A. D. Conder, J.-M. G. D. Nicola, P. D. Nicola, C. Haefner, J. M. Halpin, M. Y. Hamamoto, J. E. Heebner, M. R. Hermann, S. I. Herriot, D. C. Homoelle, D. H. Kalantar, T. E. Lanier, K. N. LaFortune, J. K. Lawson, R. R. Lowe-Webb *et al.*, Spatio-temporal focal spot characterization and modeling of the NIF ARC kilojoule picosecond laser, Appl. Opt. **60**, 2288 (2021).

[49] M. Bowers, J. Wisoff, M. Herrmann, T. Anklam, J. Dawson, J.-M. D. Nicola, C. Haefner, M. Hermann, D. Larson, C. Marshall, B. V. Wonterghem, and P. Wegner, Status of NIF laser and high power laser research at LLNL, in *High Power Lasers for Fusion Research IV*, High Power Lasers for Fusion Research Conference Series, Vol. 10084 (SPIE, Bellingham, WA, 2017), p. 1008403.

[50] J. M. D. Nicola, S. T. Yang, C. D. Boley, J. K. Crane, J. E. Heebner, T. M. Spinka, P. Arnold, C. P. J. Barty, M. W. Bowers, T. S. Budge, K. Christensen, J. W. Dawson, G. Erbert, E. Feigenbaum, G. Guss, C. Haefner, M. R. Hermann, D. Homoelle, J. A. Jarboe, J. K. Lawson *et al.*, The commissioning of the advanced radiographic capability laser system: Experimental and modeling results at the main laser output, in *High Power Lasers for Fusion Research III*, High Power Lasers for Fusion Research Conference Series, Vol. 9345 (SPIE, Bellingham, WA, 2015), p. 93450I.

[51] Z. Wu, A. Alorf, T. Yang, L. Li, and Y. Zhu, Robust x-ray sparse-view phase tomography via hierarchical synthesis convolutional neural networks, arXiv:1901.10644 (2019).

[52] J. Derouillat, A. Beck, F. Pérez, T. Vinci, M. Chiaramello, A. Grassi, M. Flé, G. Bouchard, I. Plotnikov, N. Aunai, J. Dargent, C. Riconda, and M. Grech, Smilei: A collaborative, open-source, multi-purpose particle-in-cell code for plasma simulation, Comput. Phys. Commun. **222**, 351 (2018).